

Statistical Reconstruction of Mars Entry, Descent, and Landing Trajectories and Atmospheric Profiles



*Space Systems Design Lab
Georgia Tech Aerospace Eng.*

**AE8900 MS Special Problems Report
Space Systems Design Lab (SSDL)
Guggenheim School of Aerospace Engineering
Georgia Institute of Technology
Atlanta, GA**

Author:
John Allen Christian, III

Advisor:
Dr. Robert D. Braun

April 27, 2007

Statistical Reconstruction of Mars Entry, Descent, and Landing Trajectories and Atmospheric Profiles

John A. Christian
Georgia Institute of Technology, Atlanta, GA, 30332-0150

Accurate post-flight reconstruction of a vehicle's trajectory during entry into a planetary atmosphere can produce a wide array of valuable information. The data collected through the reconstruction of entry, descent, and landing (EDL) system performance enables the quantification of performance margins for future systems. Beyond the engineering knowledge gained through trajectory reconstruction, the results may also be used by planetary scientists to generate an accurate atmospheric profile. A computer tool was developed to facilitate the rapid analysis of data gathered during entry. Emphasis was placed on making the tool flexible and capable of easily incorporating different types of data. These data are used to provide an accurate reconstruction through the use of an Extended Kalman Filter (EKF). In its present form, the filter propagates the mean state forward using a three degree-of-freedom dynamic model and is capable of handling data from accelerometers and altimeters. The tool is validated against previous trajectory and atmosphere reconstructions that were performed for the Mars Pathfinder mission.

Nomenclature

| | | | |
|--------------|--|--------------|---------------------------------------|
| g | = local acceleration due to gravity | M | = mean molecular weight |
| h | = altitude | M_∞ | = free-stream Mach number |
| m | = mass | \mathbf{P} | = state covariance matrix |
| p | = pressure | \mathbf{Q} | = state noise covariance matrix |
| q | = dynamic pressure | \mathbf{R} | = measurement covariance matrix |
| \mathbf{v} | = measurement noise vector | R | = universal gas constant |
| \mathbf{w} | = state noise vector | T | = temperature |
| \mathbf{x} | = deviation in state vector from nominal | V_i | = inertial velocity |
| \mathbf{z} | = observation vector | V_r | = relative velocity |
| | | \mathbf{X} | = full state vector |
| A_A | = axial acceleration | α_T | = total angle of attack |
| A_N | = normal acceleration | γ | = relative flight path angle (+ down) |
| A_X | = acceleration in the x-direction | γ_i | = inertial flight path angle (+ down) |
| A_Y | = acceleration in the y-direction | θ | = planetcentric longitude |
| C_A | = axial force coefficient | ρ | = local density |
| C_N | = normal force coefficient | ρ_0 | = density at h=0 km |
| C_D | = drag coefficient | σ | = bank angle |
| C_L | = lift coefficient | ϕ | = planetcentric latitude |
| D | = drag force | ψ | = relative heading angle |
| F_A | = axial force | ψ_i | = inertial heading angle |
| F_N | = normal force | ω | = planet rotation rate |
| H | = atmospheric scale height | | |
| \mathbf{H} | = measurement sensitivity matrix | Φ | = state transition matrix |
| \mathbf{K} | = Kalman gain | | |
| L | = lift force | | |
| L/D | = lift-to-drag ratio | | |

I. Introduction

The use of measurements taken during entry, descent, and landing (EDL) is an established method for accurate post-flight reconstruction of a vehicle's trajectory during entry into a planetary atmosphere.¹⁻⁵ Many data types, such as inertial acceleration measurements from accelerometers, are commonly available for use in these analyses. Further, methods exist to leverage the data collected to create an estimate of the atmospheric profile encountered by the vehicle.⁶⁻⁸ This report presents a review of these methods and discusses their incorporation into a computer tool for rapid trajectory and atmospheric reconstruction.

The tool developed here is written in MATLAB and employs an Extended Kalman Filter (EKF) to incorporate measurement data. While other methods have been proposed and implemented in past studies,^{4,8} the use of an EKF allows for an estimation of uncertainty in the reconstructed trajectory and atmosphere. This method is also capable of seamlessly incorporating many different measurement types.

This paper begins with a review of the theory and mathematics that form the underpinnings of the chosen trajectory reconstruction technique. Once this foundation is laid, the methodology and procedure used is investigated in more detail. The report is concluded with a case study where the tool is applied to the Mars Pathfinder case.

II. Overview of Trajectory Types

Three types of entry trajectories are discussed throughout this study. The relationship between these three trajectory types is shown in Fig. 1. The true trajectory is the path actually taken by the entry vehicle. The state variables along this path will never actually be known; they may only be estimated. The nominal trajectory, on the other hand, represents the trajectory predicted by the analyst's tools without the incorporation of additional data. This is the expected path of the entry vehicle. Fortunately, however, data is often available that allows for improvement of the nominal trajectory. Through taking measurements, parameters related to the true trajectory may be estimated. By intelligently incorporating these data, the analyst may improve the estimate of the entry vehicle's trajectory, resulting in the best estimated trajectory.

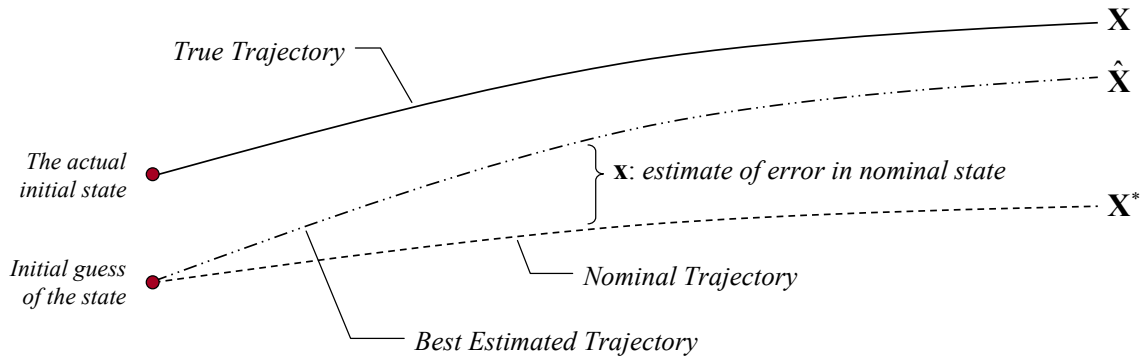


Fig. 1 Relationship between the true, nominal, and best estimated trajectory.

The full state used in this analysis is a six-element vector, \mathbf{X} , with state variables of radius, r ; planetcentric longitude, θ ; planetcentric latitude, ϕ ; relative velocity, V_r ; relative flight path angle, γ ; and relative heading angle, ψ . The difference between the nominal trajectory and best estimated trajectory at any point along the trajectory is given by \mathbf{x} . Note the slight difference in nomenclature used for the full state vector (indicated by a capital letter) and the error in the state vector (indicated by a lowercase letter).

III. Theoretical Background

The discussion of the theoretical and mathematical background is divided into four parts. First is a review of the equations of motion for planetary entry used to propagate the state variables forward in time. These equations form the foundation for many of the later analyses. This is followed by a definition of the state transition matrix as well as considerations associated with the numerical computation of this matrix. Thirdly, the measurement sensitivity matrix

is presented and example formulations are derived for common EDL measurement types. Finally, all of these topics are combined in the presentation of EKF theory.

A. Equations of Motion

Entry vehicle dynamics are modeled using the three degree-of-freedom (3-DOF) equations of motion. These equations assume point mass dynamics occurring over a rotating planet with the atmosphere fixed to the planet surface (i.e. no winds). The 3-DOF equations of motion are as follows:

$$\dot{r} = -V_r \sin(\gamma) \quad (1)$$

$$\dot{\theta} = \frac{\cos(\gamma)\cos(\psi)}{r \cos(\phi)} V_r \quad (2)$$

$$\dot{\phi} = \frac{\cos(\gamma)\sin(\psi)}{r} V_r \quad (3)$$

$$\dot{V}_r = -\frac{D}{m} + g \sin(\gamma) - \omega^2 r \cos(\phi) (\sin(\gamma)\cos(\phi) + \cos(\gamma)\sin(\phi)\sin(\psi)) \quad (4)$$

$$\dot{\gamma} = \left(\frac{1}{V_r} \right) \left[-\frac{L}{m} \cos(\sigma) + g \cos(\gamma) - \frac{V_r^2}{r} \cos(\gamma) - 2\omega V_r \cos(\phi) \cos(\psi) - \omega^2 r \cos(\phi) (\cos(\gamma)\cos(\phi) - \sin(\gamma)\sin(\phi)\sin(\psi)) \right] \quad (5)$$

$$\dot{\psi} = \left(\frac{1}{V_r} \right) \left[\frac{L \sin(\sigma)}{m \cos(\gamma)} - \frac{V_r^2}{r} \cos(\gamma) \cos(\psi) \tan(\phi) - 2\omega V_r (\tan(\gamma) \cos(\phi) \sin(\psi) + \sin(\phi)) - \frac{\omega^2 r}{\cos(\gamma)} \sin(\phi) \cos(\phi) \cos(\psi) \right] \quad (6)$$

See the nomenclature section for a description of each of the variables in Eq (1) – Eq. (6). Note that the use of planetcentric longitude/latitude allows for the use of the spherical equations of motion over a non-spherical planet (i.e. the radius of the planet is free to vary with latitude and longitude). These equations of motion are compiled from a number of sources⁹⁻¹¹ to achieve the desired combination of assumptions and variables. Changes are also made to account for the positive-down flight path angle convention used in this paper.

Because Eq (1) – Eq. (6) are derived relative to a rotating planet, inertial state variable values (velocity, flight path angle, and heading angle) must be converted to the planet fixed frame. The conversion between the inertial and relative frames for these state variables is as follows:

$$V_r = \left[(V_i \cos(\psi_i) \cos(\gamma_i) - r \cos(\phi) \omega)^2 + (V_i \sin(\psi_i) \cos(\gamma_i))^2 + (V_i \sin(\gamma_i))^2 \right]^{1/2} \quad (7)$$

$$\gamma = \frac{\pi}{2} - \tan^{-1} \left(\frac{\left[(V_i \cos(\psi_i) \cos(\gamma_i) - r \cos(\phi) \omega)^2 + (V_i \sin(\psi_i) \cos(\gamma_i))^2 \right]^{1/2}}{|V_i \sin(\gamma_i)|} \right) \quad (8)$$

$$\psi = \tan^{-1} \left(\frac{V_i \sin(\psi_i) \cos(\gamma_i)}{V_i \cos(\psi_i) \cos(\gamma_i) - r \cos(\phi) \omega} \right) \quad (9)$$

Finally, it is important to note the difference between the heading angle, ψ , and the azimuth angle. The azimuth angle is a commonly provided input and the assumed convention is that it is measured clockwise from north. The heading angle, however, is measured counterclockwise from east. Therefore, it is easy to see that the conversion between azimuth and heading angle is given by the following expression:

$$\psi = 90^\circ + (360^\circ - Azimuth) \quad (10)$$

B. State Transition Matrix

In many cases, it is desirable to map error in the vehicle's state vector at one time, t_0 , to a later time in the trajectory, t_1 . While the actual trajectory may be highly nonlinear, it is usually possible to assume the errors behave in a linear fashion as long as they remain sufficiently small. Under this assumption, the equations of motion may be linearized by taking a series expansion about a reference trajectory and retaining only the first-order terms.¹² The deviation vector, \mathbf{x} , (a six-vector of the deviation in the full state vector, \mathbf{X}) may then be mapped from time t_0 to t_1 using the following expression:

$$\mathbf{x}(t_1) = \Phi(t_1, t_0)\mathbf{x}(t_0) \quad (11)$$

The 6x6 matrix shown in Eq. 11, Φ , is a Jacobian that is frequently called the state transition matrix in this context. This matrix consists of the partial derivative of each state vector component at t_1 with respect to all of the initial state vector components.

$$\Phi(t_1, t_0) = \begin{bmatrix} \frac{\partial x_1(t_1)}{\partial x_1(t_0)} & \frac{\partial x_1(t_1)}{\partial x_2(t_0)} & \dots & \frac{\partial x_1(t_1)}{\partial x_6(t_0)} \\ \frac{\partial x_2(t_1)}{\partial x_1(t_0)} & \ddots & & \\ \vdots & & \ddots & \vdots \\ \frac{\partial x_6(t_1)}{\partial x_1(t_0)} & \dots & \frac{\partial x_6(t_1)}{\partial x_6(t_0)} \end{bmatrix} \quad (12)$$

The tool developed here numerically calculates each partial derivative using forward finite differencing. Recall that the forward finite differencing formula may be derived by expanding the function $F(x+h)$ as a Taylor series expansion. If the step size, h , is assumed to be very small, the function may be truncated and the higher order terms can be lumped into a placeholder, θ . Rearranging the truncated series expansion yields the familiar forward finite differencing formula:

$$F' = \frac{F(x+h) - F(x)}{h} + \frac{\theta(h^2)}{h} \quad (13)$$

For the purposes of calculating Φ , the step size is estimated as a 0.01% of the state variable being perturbed or $1e-4$, whichever is smaller. Each term in Φ is, therefore, calculated by perturbing the trajectory state variables one-by-one at t_0 (using the appropriate h) and observing the change it creates in the trajectory at t_1 .

C. Measurement Sensitivity Matrix

In addition to mapping errors in the state variables from t_0 to t_1 , it is also desirable to know how errors in the state vector relate to errors in measurements, \mathbf{z} . For the purposes of this discussion, \mathbf{z} is assumed to be an $n \times 1$ vector representing the errors of n different observation types. It is important to note that measurement errors are expressed as the difference between the observed and computed values (i.e. observed minus computed). It is assumed that the observations are linearly related to the state by the following expression:

$$\mathbf{z} = \mathbf{H}\mathbf{x} + \mathbf{v} \quad (14)$$

Here, \mathbf{x} is the true, unknowable deviation vector and \mathbf{v} is a random vector (mean of zero) that represents the error in the measurements. The $n \times 6$ matrix shown in Eq. (14), \mathbf{H} , is the measurement sensitivity matrix. Each row of this matrix is formed by taking the partial derivative of a given measurement type with respect to each of the state vector components at a specified time. Clearly, the \mathbf{H} matrix is problem specific and depends on the data types that are used. Two common examples in EDL reconstruction are presented here. The first is a 1×6 matrix where only axial acceleration measurements are incorporated to improve the state:

$$\mathbf{H} = \begin{bmatrix} \frac{\partial A_A}{\partial r} & \frac{\partial A_A}{\partial \theta} & \frac{\partial A_A}{\partial \phi} & \frac{\partial A_A}{\partial V_r} & \frac{\partial A_A}{\partial \gamma} & \frac{\partial A_A}{\partial \psi} \end{bmatrix} \quad (15)$$

$$\mathbf{H} = \begin{bmatrix} \frac{1}{2m} V_r^2 C_D S \left(-\frac{\rho}{H} \right) & 0 & 0 & \frac{1}{m} \rho V_r C_D S & 0 & 0 \end{bmatrix} \quad (16)$$

The next example is a 2×6 matrix where only altimeter data (altitude and altitude rate) is being used to improve the state. This matrix is as follows:

$$\mathbf{H} = \begin{bmatrix} \frac{\partial h}{\partial r} & \frac{\partial h}{\partial \theta} & \frac{\partial h}{\partial \phi} & \frac{\partial h}{\partial V_r} & \frac{\partial h}{\partial \gamma} & \frac{\partial h}{\partial \psi} \\ \frac{\partial \dot{h}}{\partial r} & \frac{\partial \dot{h}}{\partial \theta} & \frac{\partial \dot{h}}{\partial \phi} & \frac{\partial \dot{h}}{\partial V_r} & \frac{\partial \dot{h}}{\partial \gamma} & \frac{\partial \dot{h}}{\partial \psi} \end{bmatrix} \quad (17)$$

$$\mathbf{H} = \begin{bmatrix} 1 & 0 & 0 & 0 & 0 & 0 \\ 0 & 0 & 0 & -\sin(\gamma) & -V_r \cos(\gamma) & 0 \end{bmatrix} \quad (18)$$

If other measurement types are desired, the appropriate \mathbf{H} matrix rows must be derived. Fortunately, the derivation of these partial derivatives is typically straightforward and may be performed analytically. The analyst is responsible for assembling the appropriate \mathbf{H} matrix for the measurement types employed in the problem. The mechanics of this process are discussed later in more detail.

D. Extended Kalman Filtering¹²⁻¹⁴

The Kalman Filter is based on a modification of Eq.11 that results in the following recursive dynamic model:

$$\mathbf{x}_{k+1} = \Phi_k \mathbf{x}_k + \mathbf{w}_k \quad (19)$$

Here, note the addition of the state noise vector, \mathbf{w}_k , with mean of zero and a covariance $\mathbf{Q}_k = E(\mathbf{w}_k \mathbf{w}_k^T)$. The ability to account for state noise is one of the major advantages of the Kalman Filter over many other filtering methods. The inclusion of state noise allows for the consideration of statistical uncertainties in the dynamics model. Furthermore, as was discussed in Section III.C, the relationship between observations and the state are given by:

$$\mathbf{z}_k = \mathbf{H}_k \mathbf{x}_k + \mathbf{v}_k \quad (20)$$

It is important to note that the observation sensitivity matrix, \mathbf{H} , in the Kalman Filter only includes observations at time k . \mathbf{H} will, therefore, have the same number of rows as types of data being processed.

Implementation of the Kalman Filter is a sequential process that occurs in two phases: 1) observation processing and 2) mapping the state and covariance forward in time. When observational data is available, the following expressions may be used to update the current estimate of the state and covariance at a given time, k :

$$\mathbf{x}_k^+ = \mathbf{x}_k^- + \mathbf{K}_k (\mathbf{z}_k - \mathbf{H}_k \mathbf{x}_k^-) \quad (21)$$

$$\mathbf{P}_k^+ = E(\mathbf{e}_k^+ \mathbf{e}_k^{+T}) = (\mathbf{I} - \mathbf{K}_k \mathbf{H}_k) \mathbf{P}_k^- (\mathbf{I} - \mathbf{K}_k \mathbf{H}_k)^T + \mathbf{K}_k \mathbf{R}_k \mathbf{K}_k^T \quad (22)$$

The matrix \mathbf{R}_k is the measurement covariance matrix defined as $\mathbf{R}_k = E(\mathbf{v}_k \mathbf{v}_k^T)$. Further, note that \mathbf{x}_k^+ is an unbiased estimator of the true state, \mathbf{x}_k , after the measurement has been processed (\mathbf{x}_k^- is the estimate prior to processing the observation). The error in the estimate after the update is given by $\mathbf{e}_k^+ = \mathbf{x}_k^+ - \mathbf{x}_k$. Within Eq. (22), the variable \mathbf{K}_k is known as the *Kalman Gain*. This matrix is selected to minimize the updated covariance by setting the differential of Eq. (22) to zero and solving for \mathbf{K}_k . The equation for the Kalman Gain is given in Eq. (23).

$$\mathbf{K}_k = \mathbf{P}_k^- \mathbf{H}_k^T (\mathbf{H}_k \mathbf{P}_k^- \mathbf{H}_k^T + \mathbf{R}_k)^{-1} \quad (23)$$

The second phase of the Kalman Filter process, propagating the state and covariance forward in time, may be accomplished using Eq. (24) and Eq. (25).

$$\mathbf{x}_{k+1}^- = \Phi_k \mathbf{x}_k^+ \quad (24)$$

$$\mathbf{P}_{k+1}^- = \Phi_k \mathbf{P}_k^+ \Phi_k^T + \mathbf{Q}_k \quad (25)$$

The algorithm for implementing a Kalman Filter is shown graphically in Fig. 2.

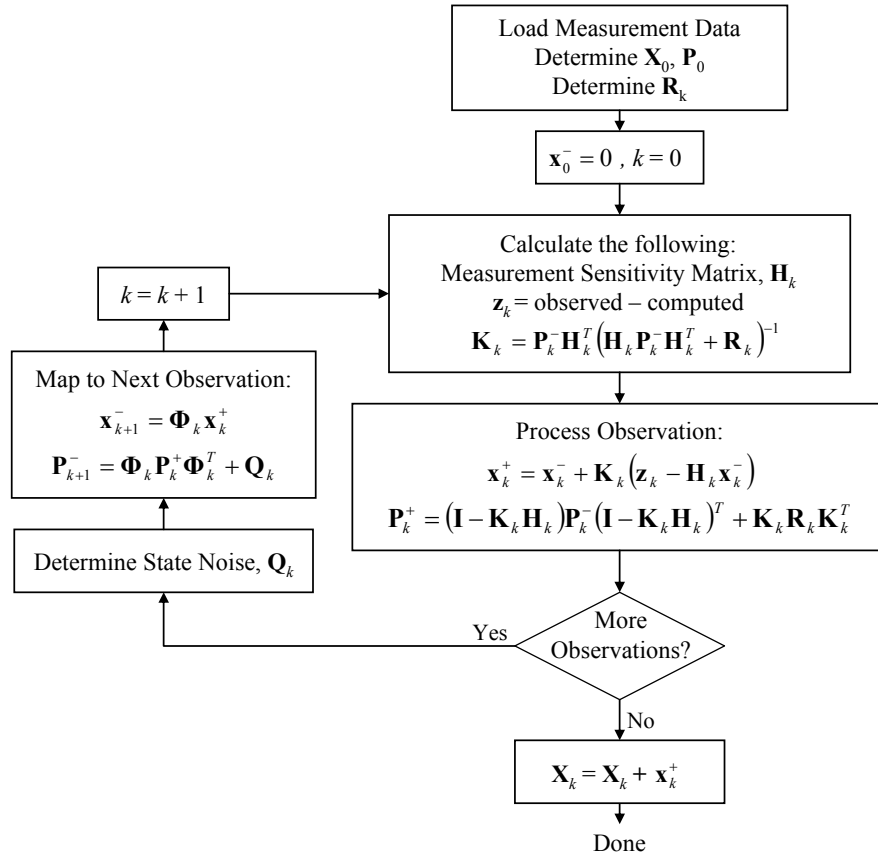


Fig. 2 Algorithm for a Kalman Filter.

IV. Implementation and Reconstruction Methodology

With the theoretical foundation established, attention is turned to the reconstruction methodology. All of the processes described below have been implemented in MATLAB R2006a and run on a desktop computer with Microsoft Windows XP Professional, Version 2002, Service Pack 2. The computational process occurs, roughly, in the same order in which it is presented in this section.

A. Generating Total Angle of Attack History

Various methods have been proposed for determining the time-history of an entry vehicle's aerodynamic performance using only accelerometer data.¹⁶ Of particular interest is an approach for estimating the time-history of the total angle of attack developed in previous studies that investigated the reconstruction of the Mars Pathfinder entry trajectory.^{4,20} The observation was made that the total angle of attack could be estimated through recognizing the following relationship:

$$\frac{C_N}{C_A} = \left(\frac{F_N}{\frac{1}{2}\rho V^2 S} \right) / \left(\frac{F_A}{\frac{1}{2}\rho V^2 S} \right) = \frac{mA_N}{mA_A} = \frac{A_N}{A_A} \quad (26)$$

In practice, one accelerometer is typically placed along the axial direction, yielding A_A directly. Two other accelerometers are placed in the plane perpendicular to the axial direction yielding A_X and A_Y , the accelerations in the x-direction and y-direction, respectively. The root-sum-square of A_X and A_Y may be then be used to compute A_N :

$$A_N = \sqrt{A_X^2 + A_Y^2} \quad (27)$$

Combining the relationships shown in Eq. (26) and Eq. (27) with vehicle aerodynamics allows the analyst to compute the time-history of total angle of attack. In many vehicle aerodynamic models, vehicle performance (C_A , C_N , C_L , C_D , C_M , etc) is given as a function of both velocity and angle of attack. Therefore, the C_N/C_A ratio may also be computed as a function of velocity and angle of attack. If an early estimate of the velocity is available through an initial integration of the axial deceleration pulse, and the C_N/C_A ratio is available from accelerometer data, the angle of attack may be computed. This procedure was performed in MATLAB through the interpolation of tabulated aerodynamic data.

B. Gravity Modeling

The current version of the reconstruction tool provides the analyst the freedom to include a gravity model with fidelity of their choosing. At the beginning of the code, the user specifies a function handle pointing to an m-file that contains the gravity model they desire to use. Currently, a simple spherical gravity model of the following form is used:

$$g = g_0 \left(\frac{r_0}{r_0 + h} \right)^2 \quad (28)$$

If the user wishes, however, they may write a more sophisticated gravity model that is latitude/longitude dependent. The simple model shown in Eq. (28) is assumed to be sufficient for these analyses.

C. Generating a Nominal Atmosphere

With a time-history of angle of attack created and a gravity model established, the next step is to generate the nominal atmosphere. This process is begun by integrating the axial deceleration pulse forward in time from the initial state. Of particular importance are the time histories of altitude and velocity generated from this procedure. Combining these results with the time history of angle of attack and the aerodynamic model, the following expression may be used to compute density:

$$\rho = \frac{2mA_A}{V^2 C_A S} \quad (29)$$

Thus, a density profile is created over the range of altitudes for which integration of the axial deceleration pulse is valid. In many missions, the accelerometer data becomes difficult to use towards the end of the trajectory as significant oscillations are introduced by a number of events that commonly occur near the end of the EDL timeline (e.g. parachute deployment, heatshield separation, lowering of lander on bridle below backshell, etc.). A different method must be used here. Depending on the data available, one of two approaches is recommended. If atmospheric measurements are available during or shortly after the EDL sequence (as is the case for Mars Pathfinder), this information may be used to reconstruct the bottom segment of the atmosphere. The density at a specified altitude (frequently the landing site) is anchored to measured values and an exponential atmosphere model is used to connect this data point to the bottom of the atmospheric profile generated through deceleration measurements. Recall the form of an exponential atmosphere,

$$\rho = \rho_0 \exp[-h/H] \quad (30)$$

where ρ_0 is the density at an altitude of zero ($h=0$) and H is the atmospheric scale height. Given the data available, it is straightforward to solve for ρ_0 and H to satisfy the conditions described above.

If no atmospheric measurements are available, a different approach must be taken. Retaining the use of the exponential model for the missing atmosphere segment, both ρ_0 and H may be approximated from the acceleration derived atmosphere model. Here, the atmospheric scale height may be estimated from a curve fit of the bottom portion of the available atmosphere model (how much of the atmospheric profile is used for this fit depends on the specific problem); ρ_0 is selected to ensure continuity between atmosphere segments.

D. Generating a Nominal Trajectory

With the time-history of the total angle of attack, gravity model, and nominal atmosphere available, the nominal trajectory may be created. Beginning with the initial state, the equations of motion shown in Eq. (1) - Eq. (6) are integrated forward in time while being subjected to the nominal density profile and the vehicle aerodynamics coupled with the time history of total angle of attack. The ‘ode45’ integration routine was implemented in MATLAB. This built-in function implements a dynamic time-step Runge-Kutta 4,5 algorithm. As is expected, the deceleration pulse created by this trajectory matches the measured data extremely well.

All trajectory analyses incorporate event modeling to allow for changes in mass (e.g. drop heatshield), drag area (e.g. deploy parachute), aerodynamics, or any other user-defined discontinuity in a vehicle parameter. Specifically, the analyst is free to divide the trajectory into an arbitrary number of flight segments and is only required to input the start and end times of each phase, the mass during each phase, the aerodynamic reference area during each phase, and a function-handle pointing to an m-file that contains the aerodynamic model for each phase. An example of how this is done is presented in the Mars Pathfinder case study located at the end of this report.

E. Implementation of the Extended Kalman Filter

Referring back to the section on Kalman filtering theory, recall that the following inputs are needed to implement an EKF:

1. *Nominal trajectory* – creation of this trajectory is as discussed in the previous section
2. *Ability to integrate equations of motion* – made possible through the gravity model, nominal atmosphere, and time-history of total angle of attack
3. *Initial state and covariance* – input that must be provided by the analyst on a problem specific basis
4. *Measurement sensitivity matrix* – requires nominal trajectory with rows constructed as discussed in Section III.C; the user must create this to match the data types used in the Kalman filter
5. *Measurement covariance* – input that must be provided by the analyst on a problem specific basis
6. *State noise* – input that must be provided by the analyst on a problem specific basis
7. *State transition matrix* – calculated numerically using the approach shown in Section III.B

In the above list, note that all the required inputs are either input by the analyst or generated using the approaches described in Section IV.A through Section IV.D. The initial state and covariance are incorporated directly by the analyst at the beginning of the code. For the other user specified inputs, the analyst specifies a function handle that points to an m-file (with time and the current state vector as inputs) which returns the desired information – either

the \mathbf{H} , \mathbf{R} , or \mathbf{Q} matrix. The analyst is free to make these matrices whatever form they wish subject to the input/output constraints specified in the code.

If only accelerometer data is available over the bulk of the trajectory, it may not be possible to create meaningful shifts in the nominal atmosphere or trajectory through the use of the EKF. In other words, the best estimated trajectory will coincide with the nominal trajectory. This is because the assumptions made in creating the nominal atmosphere will result in a nominal deceleration pulse that is always nearly identical to the measured deceleration pulse. Despite this limitation, the EKF remains an effective way to investigate the uncertainty in each of the states throughout the trajectory. Further, if non-accelerometer data is available (e.g. altimeter data, spacecraft-to-spacecraft radiometric data), the EKF is capable of appropriately shifting the trajectory states to better agree with the measured data.

Finally, care must be taken when implementing the EKF. If measurements cause large deviations from the nominal, the error in the states may become unstable when integrated over the entire descent trajectory – especially if these errors are introduced early in the process. In some cases, the introduction of additional state noise helps address this problem.

F. Atmosphere Reconstruction

After implementation of the EKF on the entry trajectory, a reconstruction of the atmosphere may be performed. As before, the density profile may be determined using Eq. (29). One of the primary challenges associated with this methodology is the difficulty associated with separating errors in density and errors in the aerodynamic modeling. This is especially problematic if no direct measures of atmospheric properties are available. Additional errors are introduced by the use of Eq. (29) when only coarse aerodynamic models are available (as is the case for the Mars Pathfinder case study discussed below). Despite these challenges with determining mean density values, the uncertainties generated by the EKF in the trajectory states (specifically altitude and velocity) may be used to generate an uncertainty in density.

With a density vs. altitude profile established, the hydrostatic equation may be integrated to determine a pressure distribution with altitude:

$$\frac{dp}{dh} = -\rho g \quad (31)$$

Ideally, direct surface pressure measurements will be available to produce a good starting point from which to begin the integration. If they are not available, a guess of the pressure must be made from other available data and the analyst's judgment. Finally, the temperature profile may be calculated at each point along the trajectory through the ideal gas law:

$$T = \left(\frac{M}{R} \right) \left(\frac{p}{\rho} \right) \quad (32)$$

where M is the mean molecular weight (assumed to be 43.2685 kg/kmol on Mars) and R is the universal gas constant (8314.34 J/kmol-K).

V. Mars Pathfinder Case Study

Data for Mars Pathfinder was compiled from a number of sources.^{3,4,16-24} Where possible, an effort was made to ensure equivalent assumptions were made before combining data. Basic vehicle parameters and the initial entry state are obtained from the Mars Pathfinder EDL reconstruction work of Spencer et al.⁴ The entry mass is assumed to be 585.3 kg with a heatshield mass of 64.4 kg and a backshell mass of 56.9 kg. The assumed entry state is as shown in Table 1. While the uncertainty in the entry states is not directly available in the literature, uncertainty data is available on the NASA Planetary Data System (PDS) at a slightly earlier epoch (July 4, 1997, 16:51:12.28 UTC, approximately 38.2 seconds prior to what is defined as entry interface).¹⁹ Assuming that these uncertainties are uncorrelated, they may be mapped forward in time (for 38.2 seconds) using the state transition matrix as is described in Eq. (25) with $\mathbf{Q}=0$. The uncertainties shown in Table 1 are generated by the author and correspond to the PDS uncertainties propagated forward in time. Analysis demonstrated that over 38.2 seconds, the error in the state grows by approximately 1.5% in the worst case. Therefore, the levels of uncertainty at both times are identical to within the precision presented.

Table 1 Summary of Mars Pathfinder entry state.

| Parameter | Mean Value ⁴ | Uncertainty (1 σ) |
|------------------------------|----------------------------------|---------------------------|
| Epoch at entry interface | July 4, 1997 16:51:50.482 UTC | Not available |
| Radial distance | 3,522.2 km | 1.7 km |
| Aerocentric latitude | 22.6303 deg | 0.04 deg |
| Aerocentric longitude | 337.9976 deg | 0.01 deg |
| Inertial velocity | 7.2642 km/s | 0.7 m/s |
| Inertial flight path angle | -14.0614 deg | 0.02 deg |
| Inertial flight-path azimuth | 253.1481 deg | 0.02 deg |

A. Analysis of Acceleration Data

Acceleration data from the accelerometers that were part of the Atmospheric Structure/Meteorology (ASI/MET) experiment is available throughout the EDL sequence. Note that for these accelerometers, lab tests demonstrated that $1\text{ g} = 9.795\text{ m/s}^2$. The measured axial acceleration is provided in Fig. 3. This axial acceleration pulse may be used to infer the timing of key events during the EDL sequence. The times of relevant EDL events are summarized in Table 2. Preprocessing of this data was performed prior to use in the reconstruction analysis performed below. This procedure removed spurious data, including spikes introduced when the gain on the accelerometer was switched.

Additionally, care must be taken when incorporating the accelerometer data. Recall that accelerometers only measure the sensed inertial acceleration. Therefore, when using equations of motion in a rotating frame, one must be careful to compare accelerations in the same frame.

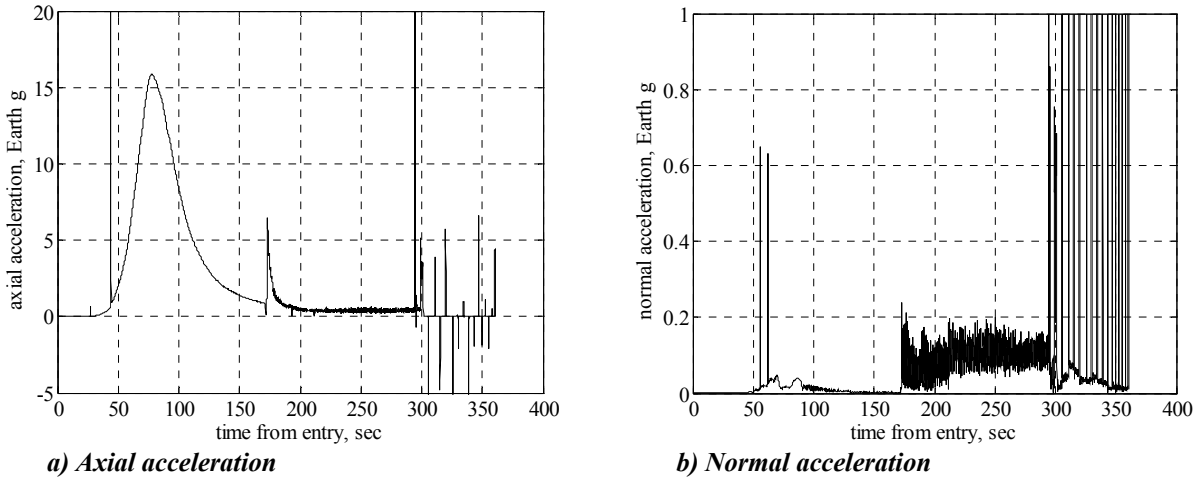


Fig. 3 Acceleration as measured by the ASI/MET accelerometers.

Table 2 Summary of key EDL events.

| Event | Time from entry, sec |
|--|----------------------|
| Entry interface ($r = 3522.2\text{ km}$) | 0.0 |
| Mortar fire | 171.4 |
| Begin parachute inflation | 172.2 |
| Parachute full inflation | 172.7 |
| Heatshield separation | 192.1 |
| Radar ground acquisition | 276.0 |
| Rocket ignition | 299.1 |
| Bridle cut | 301.3 |
| Touchdown (first bounce) | 305.0 |

B. Creation of Flight Segments

The Mars Pathfinder entry trajectory was divided into three flight segments using the approach described in Section IV.D. These three flight segments are defined by the user-defined inputs described in Table 3.

Table 3 Mars Pathfinder flight segments.

| | start time | end time | mass | Aerodynamics |
|------------------|------------|-----------|----------|---------------------|
| Flight Segment 1 | 0 sec | 172.2 sec | 585.3 kg | capsule |
| Flight Segment 2 | 172.2 sec | 192.1 sec | 585.3 kg | capsule + parachute |
| Flight Segment 3 | 192.1 sec | 297 sec | 520.9 kg | capsule + parachute |

Flight segment 1 defines the vehicle characteristics from entry through the beginning of parachute inflation. The entry vehicle aerodynamic database used during this portion of flight is as described in the literature. Tabular data of the Mars Pathfinder capsule aerodynamics are available and the data used are presented in Table 4. These data were incorporated into a MATLAB m-file and linear interpolation was performed based on inputs of angle of attack and velocity. Linear interpolation was chosen over other interpolation methods (such as Hermite cubic) for computational speed.

Table 4 Mars Pathfinder capsule aerodynamics.²²

| Angle of Attack, deg | M_∞ | C_N | C_A | C_N/C_A |
|----------------------|------------|---------|--------|-----------|
| 0 | 31.6 | 0.00000 | 1.6984 | 0.00000 |
| 0 | 22.3 | 0.00000 | 1.7290 | 0.00000 |
| 0 | 9.4 | 0.00000 | 1.6393 | 0.00000 |
| 0 | 1.9 | 0.00000 | 1.3079 | 0.00000 |
| ----- | | | | |
| 2 | 39.3 | 0.00749 | 1.6597 | 0.00451 |
| 2 | 36.7 | 0.00358 | 1.6796 | 0.00213 |
| 2 | 31.6 | 0.00238 | 1.6943 | 0.00140 |
| 2 | 27.7 | 0.00623 | 1.7138 | 0.00364 |
| 2 | 22.3 | 0.00621 | 1.7208 | 0.00361 |
| 2 | 20.9 | 0.00557 | 1.7168 | 0.00324 |
| 2 | 18.3 | 0.00344 | 1.7141 | 0.00201 |
| 2 | 16.0 | 0.00173 | 1.6999 | 0.00102 |
| 2 | 14.0 | 0.00262 | 1.6740 | 0.00157 |
| 2 | 12.2 | 0.00322 | 1.6547 | 0.00195 |
| 2 | 9.4 | 0.00364 | 1.6382 | 0.00222 |
| 2 | 1.9 | 0.00480 | 1.3069 | 0.00367 |
| ----- | | | | |
| 5 | 39.3 | 0.01852 | 1.6508 | 0.01122 |
| 5 | 36.7 | 0.01121 | 1.6595 | 0.00676 |
| 5 | 31.6 | 0.01047 | 1.6616 | 0.00630 |
| 5 | 27.7 | 0.01451 | 1.6821 | 0.00863 |
| 5 | 22.3 | 0.01425 | 1.6877 | 0.00844 |
| 5 | 18.3 | 0.01104 | 1.6804 | 0.00657 |
| 5 | 16.0 | 0.00996 | 1.6679 | 0.00597 |
| 5 | 14.0 | 0.00859 | 1.6563 | 0.00519 |
| 5 | 12.2 | 0.00890 | 1.6418 | 0.00542 |
| 5 | 9.4 | 0.00971 | 1.6278 | 0.00597 |
| 5 | 1.9 | 0.01190 | 1.3027 | 0.00913 |
| ----- | | | | |
| 11 | 39.3 | 0.04517 | 1.5896 | 0.02842 |
| 11 | 36.7 | 0.03592 | 1.5767 | 0.02278 |
| 11 | 22.3 | 0.03571 | 1.5954 | 0.02238 |
| 11 | 1.9 | 0.02607 | 1.2813 | 0.02035 |

Flight segment 2 begins at parachute inflation and lasts through heatshield separation. To remain consistent with previous studies, parachute drag coefficients of $C_{D0}=0.41^{18}$ and $C_{D0}=0.50^4$ were investigated. During inflation, the drag generated by the parachute is modeled through the inflation curve method:

$$F_P = qC_{D0}S_0 \left(\frac{t - t_{SI}}{t_{FI} - t_{SI}} \right)^n \quad (33)$$

where t_{SI} is the inflation start time and t_{FI} is the time of full inflation. Through inspection of the accelerometer data, it was determined that the inflation time was approximately 0.53 seconds.

Flight segment 3 begins after the 64.4 kg heatshield is dropped and the vehicle mass is reduced from 585.3 kg to 520.9 kg. During this segment, drag is produced by both the parachute and capsule. This phase is concluded at 297 seconds after entry interface, just prior to retrorocket ignition.

C. Reconstruction of Total Angle of Attack

Using the measured acceleration data shown in Fig. 3 and the aerodynamics specified in Table 4, the time history of total angle of attack may be computed. Fig. 4 shows a comparison of the normal-to-axial acceleration ratio developed using the techniques described in this study with data available in the literature. Fig. 5 provides a similar comparison for total angle of attack.

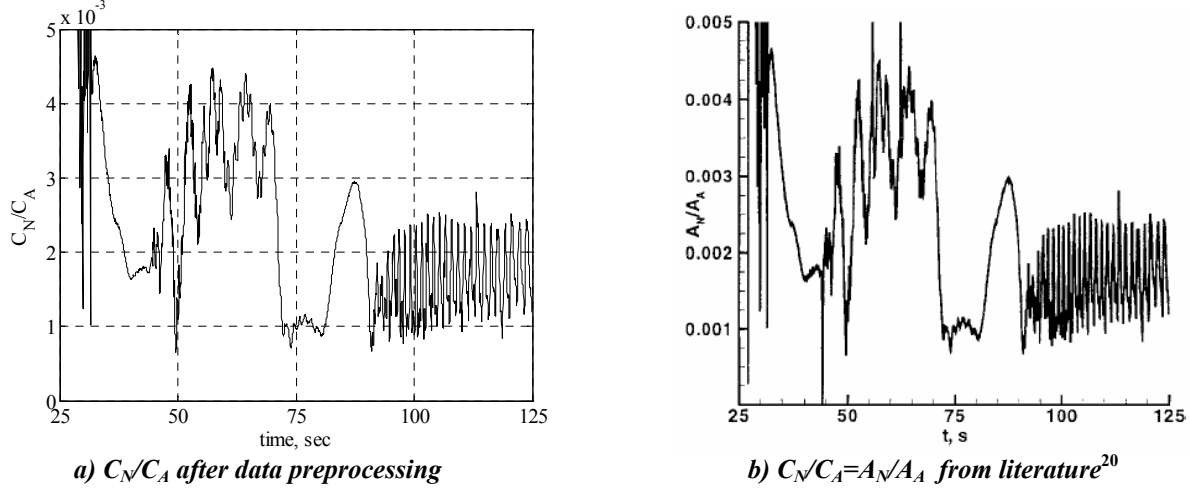


Fig. 4 Comparison of time history of normal-to-axial acceleration ratio.

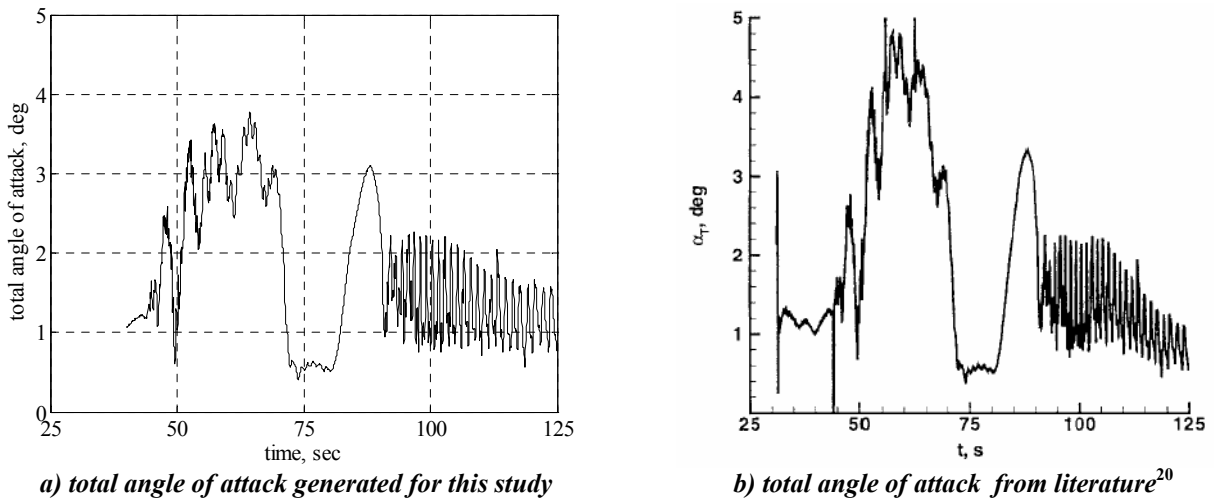


Fig. 5 Comparison of time history of total angle of attack.

After reviewing the total angle of attack data shown in Fig. 5, the limitations of the aerodynamic model presented in Table 4 become apparent. The relatively coarse resolution of aerodynamic data combined with the linear interpolation between available data points likely contributes to the difference seen in angle of attack between 50 seconds and 70 seconds. The predicted angle of attack before 50 seconds and after 70 seconds shows good agreement with the values presented in the literature.

D. Creation of Mars Pathfinder Nominal Atmosphere

The nominal atmosphere for Mars Pathfinder may now be computed as discussed in Section IV.C. The altitude and velocity profiles may be estimated through propagating the measured axial deceleration pulse forward in time, while the axial force coefficient, C_A , is estimated based on the velocity, angle of attack (Fig. 5), and assumed aerodynamic database (Table 4). Fortunately, Mars Pathfinder took atmospheric measurements shortly after landing. The measured density at the surface was approximately 0.0176 kg/m^3 .²⁴ To ensure continuity between atmosphere segments, the exponential atmosphere model used to estimate the density at low altitudes requires an atmospheric scale height of 13,787 km. The nominal density profile generated using the techniques discussed in Section IV.C is as shown in Fig. 6. Additionally, this figure provides a comparison of the nominal density profile with the post-flight density profile available on the NASA PDS constructed from ASI/MET data.²⁵

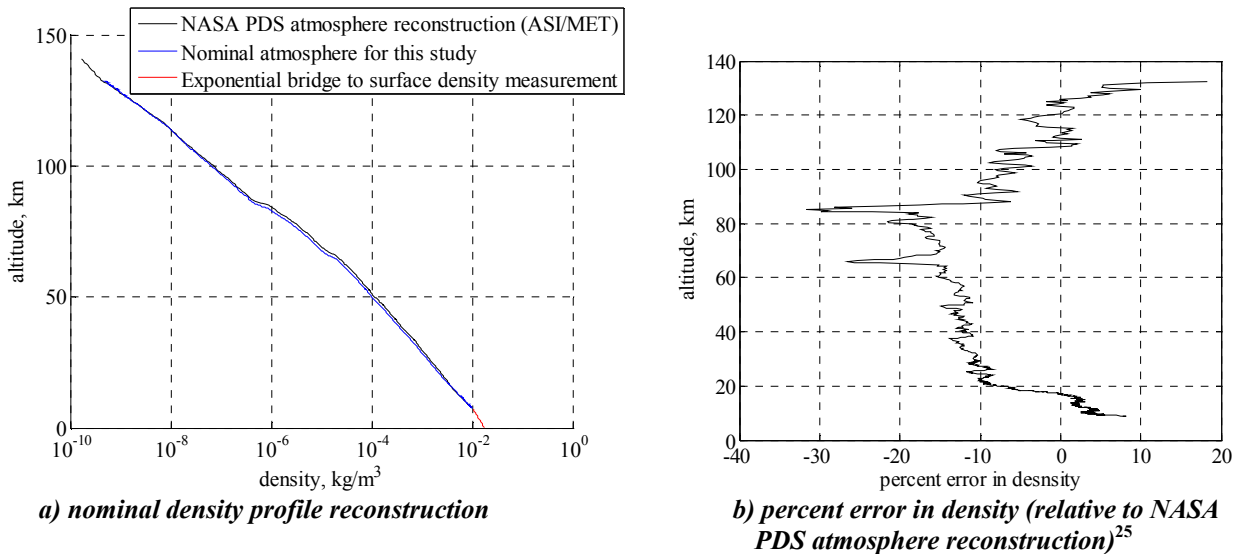
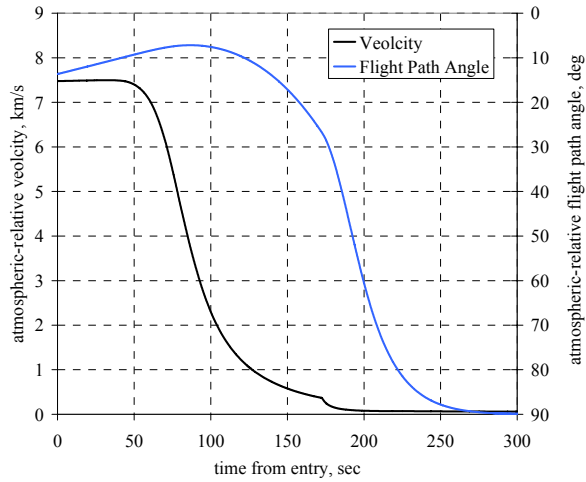


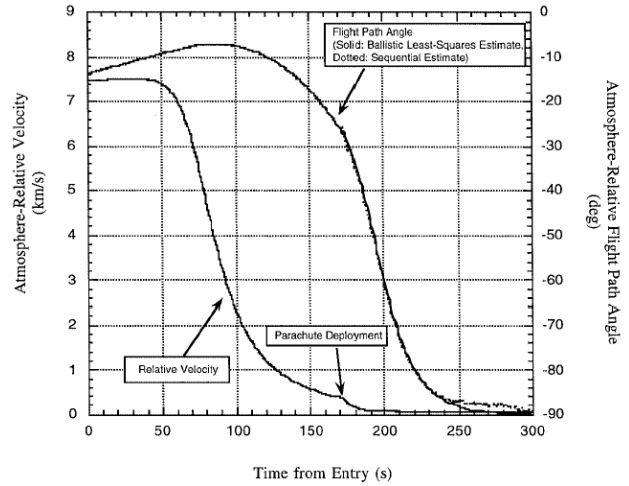
Fig. 6 Nominal density profile reconstruction and comparison with results from literature.

E. Creation of Mars Pathfinder Nominal Trajectory

The atmospheric, aerodynamic, and event data presented above are sufficient to construct a nominal trajectory. This trajectory is created by integrating the initial conditions shown in Table 1 forward in time. Because the Pathfinder entry vehicle was spin stabilized at a rate of approximately 2 rpm, perturbations in the ballistic trajectory caused by normal acceleration were assumed to cancel each other out. The results obtained for the nominal trajectory in this study, along with a comparison with results from the literature, are shown in Fig. 7 and Fig. 8.

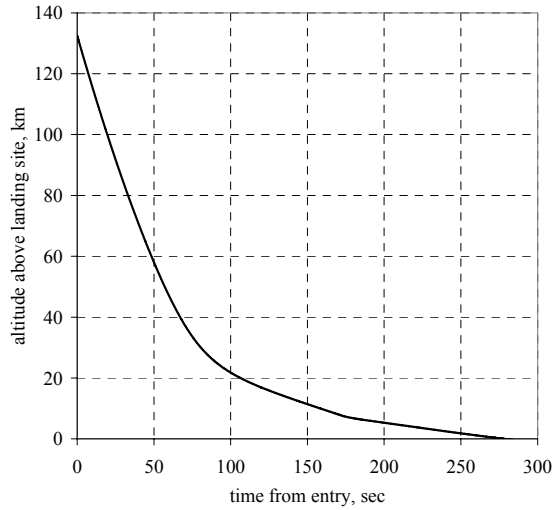


a) nominal velocity and flight path angle

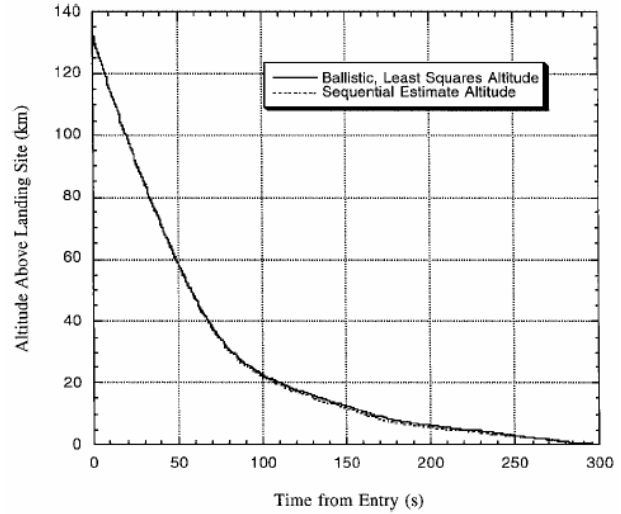


b) velocity and flight path angle from literature⁴

Fig. 7 Comparison of nominal atmosphere-relative velocity and flight path angle with results from literature.



a) nominal altitude above landing site



b) altitude above landing site from literature⁴

Fig. 8 Comparison of nominal altitude with results from literature.

F. Implementation of Extended Kalman Filter

An EKF was implemented to incorporate the accelerometer data and altimeter data recorded during the Mars Pathfinder entry. The accelerometer data is available at sampling rate 32 Hz and altimeter data is available at 1 Hz. The instrument characteristics used to generate the measurement covariance matrix, \mathbf{R} , are as shown in Table 5.

Table 5 Summary of assumed instrument performance.

| Instrument | Description | Measurement | Measurement Uncertainty |
|------------------------------|-----------------------|---------------------|--------------------------|
| Accelerometers ²⁶ | Allied Signal QA-3000 | Sensed Acceleration | 1,500 μg -rms |
| Altimeter | Honeywell HG8505DA | Altitude | 0.3 m |
| | | Altitude Rate | 1 m/s |

Prior to parachute deployment, the standard deviation in accelerometer measurements is assumed to be approximately equal to the instrument measurement uncertainty at the stated sampling rate (1,500 μg).²⁶ After the parachute is deployed, significant oscillations in the accelerometer data are observed throughout the remainder of the trajectory. From this point forward, based on inspection of the apparent noise level in the data, a standard deviation of 0.1 g is assumed.

In this problem, the EKF is implemented in two phases. From entry interface until the time the altimeter acquires the ground ($t = 0$ -277 seconds), only accelerometer data is used and measurements are incorporated using the \mathbf{H} matrix shown in Eq. (16). From altimeter ground acquisition (277 seconds) until just prior to retrorocket firing (298 seconds), altimeter data is used. No altimeter data was available to the author beyond 298 seconds after entry interface. The altimeter measurements are incorporated into the EKF using the \mathbf{H} matrix shown in Eq. (18).

Implementation of the accelerometer data yields the results shown below in Fig. 9. The nominal trajectory is shown in black and the 1- σ error bands are shown in green.

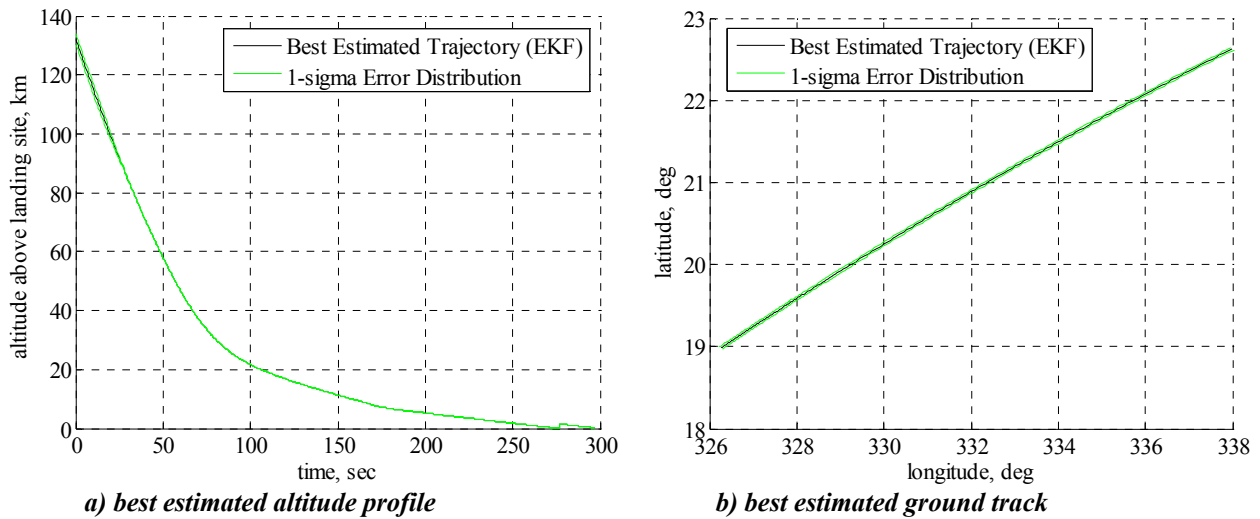


Fig. 9 Time-history of selected states from the best estimated trajectory.

Comparison with the trajectories from the literature (see Fig. 7 and Fig. 8) shows excellent agreement. To achieve a better comparison than is possible by visual inspection, the data for the (sequential) best estimated trajectory developed by Spencer et al. in 1999⁴ was obtained by the author. This information allowed for a more detailed comparison of the results from these two studies. This comparison is shown in Fig. 10.

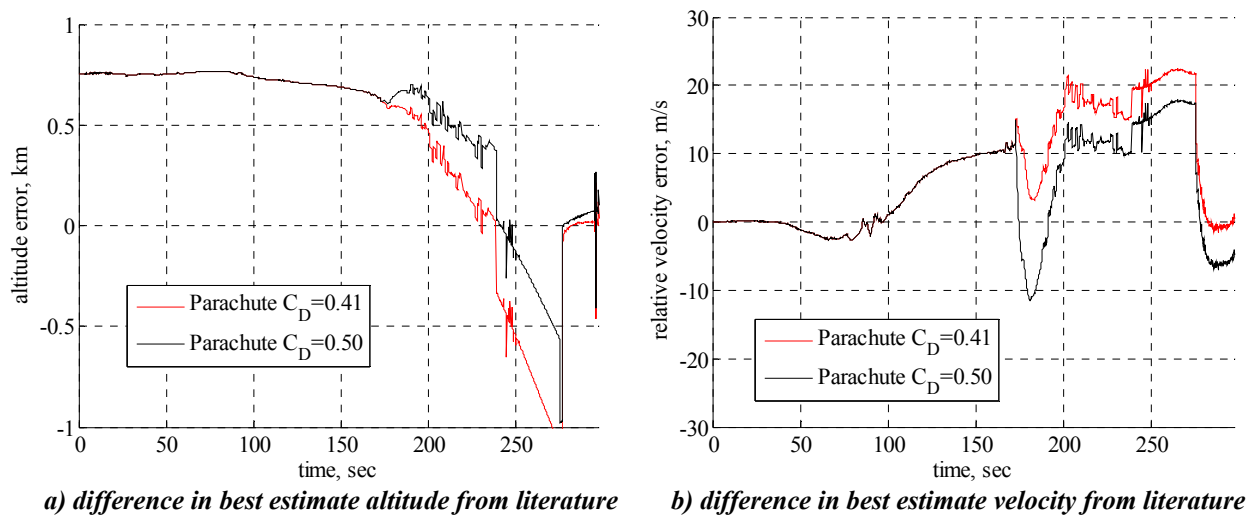


Fig. 10 Absolute difference in altitude and velocity between the results of this study and those found by Spencer et al. in 1999.⁴

The results shown in Fig. 10 compare the error observed for two different parachute drag coefficients. If a parachute C_{D0} of 0.50 is used (the assumption made by Spencer et al.), then the maximum difference in position is about 750 m and the maximum error in velocity is about 18 m/s. The observed differences become greater if a parachute C_{D0} of 0.41 is used instead (the reconstructed Pathfinder DGB performance by Desai et al. in 2005).¹⁸

The difference between the results of this study and those found by Spencer et al. are small – on the order of 100s of meters in altitude and 10s of m/s in velocity. Of particular interest is the approximately constant bias in altitude of ~ 750 m seen throughout the direct comparison between the two trajectories (the black line in Fig. 10). The observed differences are possibly introduced by a number of sources. First, note that the sequential estimator employed by Spencer et al. utilized noncoherent Doppler data collected during entry in addition to accelerometer and altimeter measurements. This data was not available for use in this study. Because only accelerometer data was available for the majority of the trajectory, the approach discussed here was not able to shift the trajectory away from the nominal estimate (i.e. no new information is available to create an appreciable shift the states between $t=0$ sec and $t=277$ sec). Note that when the altimeter data becomes available the difference between the method presented here and that presented by Spencer et al. collapses to zero.

A second reason that likely contributes to the observed error is the choice of reference from which altitude is measured. While the label attached to the data used for comparison states that all altitudes are given with respect to elevation above the landing site, it is clear that there is an initial condition difference of approximately 750 m between the Spencer et al sequential estimation and the stated altitude at entry interface if a spherical planet is assumed. If, however, a non-spherical planet was used, this initial condition error may be eliminated. If such a shift were to be made, it would result in a difference similar to that shown by the red line in Fig. 11 (assuming a parachute $C_{D0}=0.50$). Unfortunately, a discussion of the planet model used (e.g. spherical, ellipsoidal, etc) was not available in the primary reference⁴ or in related literature by the same authors.^{17,21}

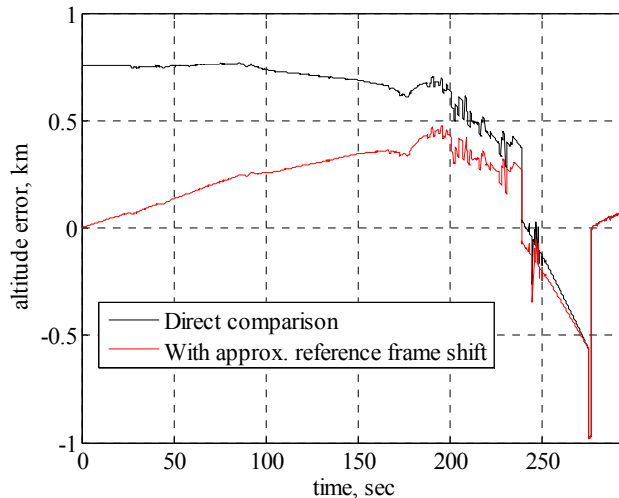


Fig. 11 Absolute difference in altitude with reference frame shift.

A third potential reason for the observed discrepancies is the aerodynamic and atmospheric assumptions made in the current analysis. First, it was assumed that the normal accelerations canceled each other out and they were not included in this analysis. Further, the aerodynamic database available was limited to the data seen in Table 4 and the resolution available here is likely much coarser than what was used by Spencer et al. Further, these aerodynamic data are only valid in the continuum regime. In future work, improvements to the current capsule aerodynamic model could be made and the effect on the trajectory assessed. Errors in the capsule aerodynamics may translate to errors in the estimated density. Additionally, a more sophisticated parachute drag model could be used to improve trajectory modeling after parachute deployment. As is clear from Fig. 6, the nominal density profile predicts an atmosphere that is too thin at higher altitude and too thick at lower altitudes. Such an offset in density helps explain some of the patterns seen in Fig. 10. At the higher altitudes, where the accelerometer data is used to compute the density, errors in the trajectory induced by density and aerodynamics errors should (mostly) cancel each other out due to the method used to compute density. Such a cancellation is not observed, however, when the vehicle enters the low-altitude exponential atmosphere at approximately 171 seconds after entry interface (when altitude = 7.65 km). Here, errors in density and aerodynamics will directly cause errors in the trajectory solution. Because the density at low altitudes is higher than predicted by NASA PDS, the drop in altitude (relative to the trajectory predicted in the

literature) is not unexpected. Additional data types may eliminate this problem. The combination of results from applying an EKF forwards and backwards along the trajectory may also work (discussed more in the Section VI).

A few additional observations may be made by zooming in on the last portion of the altitude vs. time plot, where results are driven by altimeter measurements (Fig. 12). The far left-hand side of Fig. 12 provides a better description of the difference between the best estimated trajectory developed in this study and the results from the literature at the point of maximum deviation between the two solutions. Further, this figure also shows how altimeter data collapses the error between the two solutions.

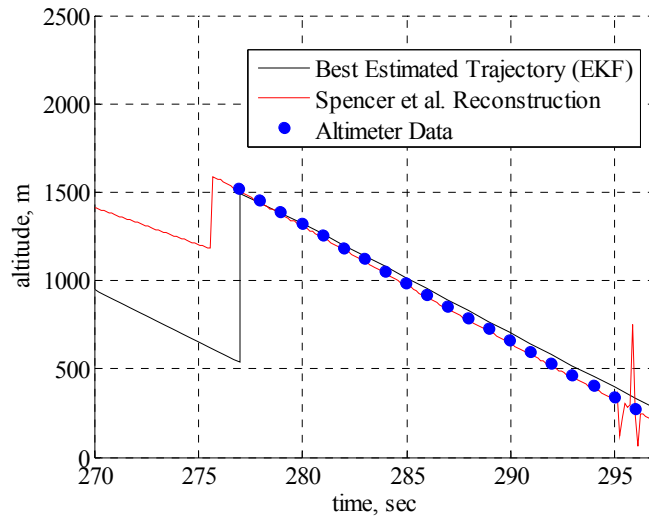


Fig. 12 Investigation of trajectory during times with operational altimeter.

Finally, the performance of this algorithm in determining the Pathfinder landing location was assessed. The landing site generated by the best estimated trajectory, along with the 1- σ error ellipse around this site, is shown in Fig. 13. The results from this study are compared to other estimates of the Pathfinder landing site made in past studies. While the trajectories showed good agreement throughout the EDL profile, a significant overshoot is observed in the final landing site estimated in this study. This error could arise from a number of sources, including the assumed atmosphere profile (Fig. 6 shows that the atmosphere is too thin throughout most of the trajectory) or vehicle aerodynamics. Additionally, it is interesting to note that both the reconstruction of Spencer et al. and the reconstruction performed in this study predict a landing site noticeably south of the actual landing site.

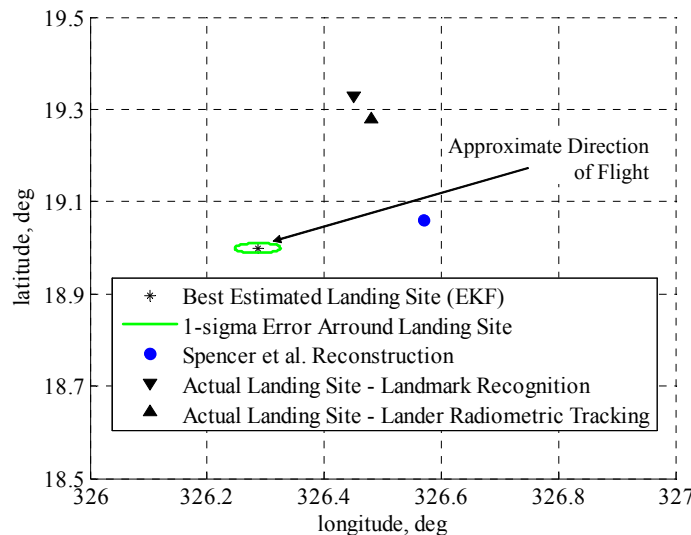


Fig. 13 Comparison of various solutions to the Pathfinder landing site.

G. Reconstruction of Atmosphere

The final step in the reconstruction process is to generate a reconstruction of the atmosphere encountered by the vehicle. This analysis is performed according to the procedure outlined in Section IV.F using the best estimated trajectory data developed above. This analysis results in no appreciable change in the mean density shown in Fig. 6 and produces a temperature profile as indicated in Fig. 14.

In performing this analysis, it was observed that the pressure and temperature profiles are extremely sensitive to small changes in density/temperature/pressure assumed at the Pathfinder landing site (if the hydrostatic equation is integrated from the surface upwards). The results appear to be much less sensitive to error if the analysis is performed in the opposite direction (i.e. integrate hydrostatic equation from entry interface to the surface). While this approach appears to be less sensitive to small errors in the initial conditions, the properties of interest must be available at entry interface.

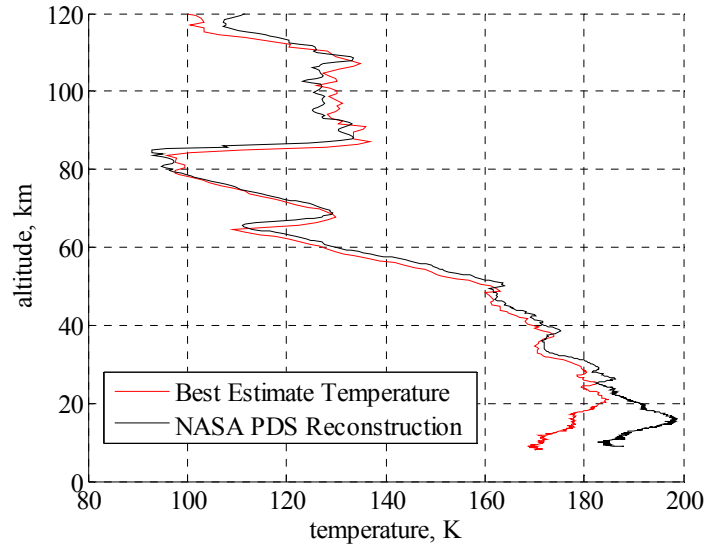


Fig. 14 Reconstruction of temperature profile with comparison to results from the literature.²⁵

VI. Future Work

A number of areas exist for future work. First and foremost, development of a robust method for implementing the EKF forwards and backwards along the trajectory should be explored. Limited success was achieved with backwards integration due to the large initial error relative to the nominal trajectory. These initial errors led to divergence of some of the states when they are propagated backwards along the entire entry trajectory (even after many test cases with various levels of state noise). The only states that could reliably be kept stable were altitude and velocity. It is postulated, therefore, that the polar-coordinate representation of the equations of motions, Eq. (1) – Eq. (6), may not be the best formulation to use with an EKF. In particular, difficulty was noticed with the sensitivity of the states to flight path angle, especially at the high velocities experienced early in the trajectory. An investigation should be performed to determine if the linearization of the error around the nominal trajectory behaves better in Cartesian coordinates. Another approach attempted for backwards implementation of the EKF was to use the known end conditions as a starting point and create a new nominal trajectory by integrating backwards. When this approach was attempted, the deceleration pulse could not easily be matched.

There is also room for improvement in the computational speed of the algorithms implemented in this tool. The current tool makes extensive use of MATLAB interpolation functions and requires frequent numerical computation of the state transition matrix. Interpolation may be sped up by replacing the standard MATLAB interpolation routines with C or FORTRAN based mex-files. Additionally, the state transition matrix need not be calculated at every time step. Modifications could be made to perform this computationally expensive operation only when necessary.

Finally, in its present form, the tool requires the analyst to run several different MATLAB scripts in a given order to generate the appropriate data files. Additionally, the user is required to develop a number of modules for any problem they wish to solve – these modules provide mission specific information such as the vehicle

aerodynamics database or the measurement covariance matrix. Much of this could be automated through a user-friendly environment

VII. Conclusions

A flexible trajectory reconstruction tool has been created. This tool is capable of simultaneously handling many different measurement types that occur over different mission phases. Additionally, the user is capable of specifying vehicle characteristics (including mass, reference area, and aerodynamics) as a function of time. This flexibility gives the user the ability to vary the fidelity of the trajectory and atmospheric reconstruction as appropriate.

The capability of this tool is, in many ways, similar to what has been developed for post-flight reconstruction of past robotic missions. The strengths of this contribution, however, lie in two areas. First and foremost, a great deal of effort has been made to make this tool as flexible and open as possible. This attribute allows for the rapid implementation of this tool to new problems. Secondly, the methodology of directly integrating the deceleration pulse to provide a good initial guess of the atmospheric profile removes many of the problems associated with attempting to reconstruct a trajectory with a poor atmosphere model.

Finally, this tool has a wide array of potential applications. The most straightforward application is use in the reconstruction of entry profiles from upcoming Mars missions such as Mars Phoenix or Mars Science Laboratory. Further, this tool may be used in conceptual design studies to determine if the performance of a proposed navigation architecture is sufficient to provide adequate state variable knowledge.

References

- ¹ Barton, R. and Ljungwe, A., "Trajectory Reconstruction Utilizing Kalman Filter Estimation Theory," *AIAA Guidance, Control, and Flight Mechanics Conference*, Hempstead, NY, 16-18 August 1971.
- ² Euler, E.A., Adams, G.L., and Hopper, F.W., "Design and Reconstruction of the Viking Lander Descent Trajectories," *Journal of Guidance and Control*, Vol. 1, No. 5, September-October 1978, pp 372-378.
- ³ Atkinson, D.H. and Kazeminejad, B., "The ESA Huygens Probe Entry and Descent Trajectory Reconstruction," *International Workshop on Planetary Probe Atmospheric Entry and Descent Trajectory Analysis and Science*, Lisbon, Portugal, 6-9 October 2003.
- ⁴ Spencer, D.A., Blanchard, R.C., Braun, R.D., Kallemeyn, P.H., and Thurman, S.W., "Mars Pathfinder Entry, Descent, and Landing Reconstruction," *Journal of Spacecraft and Rockets*, Vol. 36, No. 3 May-June 1999, pp 357-366.
- ⁵ Deasi, P.N., Blanchard, R.C., and Powell, R.W., "Entry Trajectory and Atmosphere Reconstruction Methodologies for the Mars Exploration Rover Mission," *International Workshop on Planetary Probe Atmospheric Entry and Descent Trajectory Analysis and Science*, Lisbon, Portugal, 6-9 October 2003.
- ⁶ Peterson, V.L., "A Technique for Determining Atmosphere Structure from Measured Accelerations of an Entry Vehicle," NASA-TN-D-2669, February 1965.
- ⁷ Sommer, S.C., Boissevain, A.G., Yee, L., and Hedlund, R.C., "The Structure of an Atmosphere from on-board Measurements of Pressure, Temperature, and Acceleration," NASA-TN-D-3933, April 1967.
- ⁸ Withers, P. and Smith, M.D., "Atmospheric Entry Profiles from the Mars Exploration Rovers Spirit and Opportunity," *Icarus*, Vol. 185, 2006, pp 133-142.
- ⁹ Vinh, N.X., Buseman, A., and Culp, R.D., *Hypersonic and Planetary Entry Flight Mechanics*, The University of Michigan Press, Ann Arbor, MI, 1980, pp 19-28.
- ¹⁰ Mease, K.D., Chen, D.T., Tandon, S., Young, D.H., and Kim, S., "A Three-Dimensional Predictive Entry Guidance Approach," *AIAA Guidance, Navigation, and Control Conference and Exhibit*, Denver, CO, 14-17 August 2000.
- ¹¹ Kipp, D.M. and Braun, R.D., "Development of Trajectory Simulation Capabilities for the Planetary Entry Systems Synthesis Tool," AE8900 MS Special Problems Report, Georgia Institute of Technology, 2005.
- ¹² Battin, R.H., *An Introduction to the Mathematics and Methods of Astrodynamics, Revised Edition*, American Institute of Aeronautics and Astronautics Education Series, Reston, VA, 1999.
- ¹³ Zarchan, P. and Musoff, H., *Fundamentals of Kalman Filtering: A Practical Approach, Second Edition*, Progress in Astronautics and Aeronautics: Vol. 208, American Institute of Aeronautics and Astronautics, Reston, VA, 2005, Chap 7.
- ¹⁴ Tapley, B.D., Schutz, B.E., and Born, G.H., *Statistical Orbit Determination*, Elsevier Academic Press, 2004, pp 199-211.
- ¹⁵ Kayton, M. and Fried, W.R., *Avionics Navigation Systems, Second Edition*, John Wiley & Sons, New York, NY, 1997, pp 72-81.
- ¹⁶ Withers, P., Towner, M.C., Hathi, B., and Zarnacki, J.C., "Analysis of Entry Accelerometer Data: A Case Study of Mars Pathfinder," *Planetary and Space Science*, Vol. 51, 2003, pp 541-561.
- ¹⁷ Vaugham, R.M., Kallemeyn, P.H., Spencer, D.A., and Braun, R.D., "Navigation Flight Operations for Mars Pathfinder," *Journal of Spacecraft and Rockets*, Vol. 36, No. 3, May-June 1999, pp 340-347.
- ¹⁸ Desai, P.N., Schofield, J.T., and Lisano, M.E., "Flight Reconstruction of the Mars Pathfinder Disk-Gap-Band Parachute Drag Coefficients," *Journal of Spacecraft and Rockets*, Vol. 42, No. 4, July-August 2005, pp 672-676.
- ¹⁹ Anon., "Mars Pathfinder EDL Derived Profiles Dataset Description," MPFL-M-ASIMET-4-DDR-EDL-V1.0, mpam_0001/document/edlhdrs, NASA Planetary Data System, July 1997.
- ²⁰ Gnoffo, P.A., Braun, R.D., Weilmuenster, K.J., Mitcheltree, R.A., Engelund, W.C., and Powell, R.W., "Prediction and Validation of Mars Pathfinder Hypersonic Aerodynamic Database," *Journal of Spacecraft and Rockets*, Vol. 36, No. 3, May-June 1999, pp 367-373.
- ²¹ Braun, R.D., Powell, R.W., Engelund, W.C., and Gnoffo, P.A., "Mars Pathfinder Six-Degree-of-Freedom Entry Analysis," *Journal of Spacecraft and Rockets*, Vol. 32, No. 6, November-December 1995, pp 993-1000.
- ²² Gnoffo, P.A., Weilmuenster, K.J., Braun, R.D., and Cruz, C.I., "Influence of Sonic-Line Location on Mars Pathfinder Probe Aerothermodynamics," *Journal of Spacecraft and Rockets*, Vol. 33, No. 2, March-April 1996, pp 169-177.

²³ Moss, J.N., Wilmoth, R.G., and Price, J.M., “DSMC Simulations of Blunt Body Flows for Mars Entries: Mars Pathfinder and Mars Microprobe Capsules,” *32nd AIAA Thermophysics Conference*, Atlanta, GA, 23-25 June 1997.

²⁴ Schofield, J.T., Barnes, J.R., Crisp, D., Haberle, R.M., Larsen, S., Magalhaes, J.A., Murphy, J.R., Seiff, A., and Wilson, G., “The Mars Pathfinder Atmospheric Structure Investigation/Meteorology (ASI/MET) Experiment,” *Science*, Vol. 278, No. 5344, December 1997, pp 1752-1758.

²⁵ “ASI/MET Derived EDL Density/Pressure/Temperature Profiles,” MPFL-M-ASIMET-4-DDR-EDL-V1.0, mpam_0001/edl_ddr, NASA Planetary Data System, April 1999.

²⁶ “Q-Flex® QA-3000 Accelerometer,” Product Data Sheet, Honeywell, August 2005.